


## Controlling $T_c$ through Band Structure and Correlation Engineering in Collapsed and Uncollapsed Phases of Iron Arsenides

Swagata Acharya<sup>✉,\*</sup>, Dimitar Pashov,<sup>1</sup> Francois Jamet<sup>✉,1</sup> and Mark van Schilfgaarde<sup>1,2</sup>  
*King's College London, Theory and Simulation of Condensed Matter, The Strand, WC2R 2LS London, United Kingdom*  
*National Renewable Energy Laboratories, Golden, Colorado 80401, USA*

 (Received 13 December 2019; revised manuscript received 26 March 2020; accepted 21 April 2020; published 11 June 2020)

Recent observations of selective emergence (suppression) of superconductivity in the uncollapsed (collapsed) tetragonal phase of  $\text{LaFe}_2\text{As}_2$  has rekindled interest in understanding what features of the band structure control the superconducting  $T_c$ . We show that the proximity of the narrow Fe- $d_{xy}$  state to the Fermi energy emerges as the primary factor. In the uncollapsed phase this state is at the Fermi energy, and is most strongly correlated and a source of enhanced scattering in both single and two particle channels. The resulting intense and broad low energy spin fluctuations suppress magnetic ordering and simultaneously provide glue for Cooper pair formation. In the collapsed tetragonal phase, the  $d_{xy}$  state is driven far below the Fermi energy, which suppresses the low-energy scattering and blocks superconductivity. A similar source of broad spin excitation appears in uncollapsed and collapsed phases of  $\text{CaFe}_2\text{As}_2$ . This suggests controlling coherence provides a way to engineer  $T_c$  in unconventional superconductors primarily mediated through spin fluctuations.

DOI: [10.1103/PhysRevLett.124.237001](https://doi.org/10.1103/PhysRevLett.124.237001)

Through careful control of growth and annealing conditions,  $\text{LaFe}_2\text{As}_2$  (LFA) can be grown in the tetragonal phase with markedly longer  $c$  axis than the value in the equilibrium “collapsed” tetragonal (CT) phase ( $c = 11.01 \text{ \AA}$ ). The “uncollapsed” tetragonal phase (UT) has  $c = 11.73 \text{ \AA}$ . Moreover, the UT phase is shown to superconduct at 12.1 K, while the CT phase is not a superconductor [1]. A parallel phenomenon was observed in undoped  $\text{CaFe}_2\text{As}_2$  (CFA). At room temperature, the equilibrium phase is UT, but it was recently shown that a CT phase can be induced by quenching films grown at high temperature [2]. In this case, the undoped CT phase superconducts with  $T_c = 25 \text{ K}$ . The UT phase does not exist at low temperature because CFA undergoes a transition from the tetragonal ( $I4/mmm$ ) to orthorhombic ( $Fmmm$ ) phase at 170 K [3], with a concomitant transition to an ordered antiferromagnetic state [4]. It is also possible to induce a CT phase at low temperature by applying pressure [5,6]: superconductivity was reported with  $T_c$  12 K at 0.3 GPa. Taken together, these findings rekindle the longstanding question as to whether universal band features can explain unconventional superconductivity.

Here we use a recently developed *ab initio* technique to show that there is indeed a universal feature, namely, incoherence originating from the Fe  $d_{xy}$  state. By “incoherence” we refer to the fuzzy spectral features and momentum-broadened spin excitation caused by enhanced single- and two-particle scattering. Superconductivity depends critically on the alignment of this state to the Fermi level. We are able to make these findings thanks to recent developments that couple (quasiparticle) self

consistent  $GW$  (QSGW) with dynamical mean field theory (DMFT) [7–10]. Merging these two state-of-the-art methods captures the effect of both strong local dynamic spin fluctuations (captured well in DMFT), and nonlocal dynamic correlation [11,12] effects captured by QSGW [13]. We use QSGW and not some other form of  $GW$ , e.g.,  $GW$  based on DFT. It has been well established that QSGW overcomes limitations of DFT- $GW$  when correlations become strong (see in particular Sec. 4 of Ref. [12]). On top of the DMFT self-energy, charge and spin susceptibilities are obtained from vertex functions computed from the two-particle Green’s function generated in DMFT, via the solutions of the nonlocal Bethe Salpeter equation. Additionally, we compute the particle-particle vertex functions and solve the linearized Eliashberg equation [9,14,15] to compute the superconducting susceptibilities and eigenvalues of superconducting gap instabilities. For CT and UT phases we use a single value for  $U$  and  $J$  (3.5 and 0.62 eV, respectively), which we obtained from bulk FeSe (and LiFeAs) within a constrained RPA implementation following Ersoy *et al.* [16]. DMFT is performed in the Fe-3d subspace, solved using a rotationally invariant Coulomb interaction generated by these  $U$  and  $J$ . The full implementation of the four-tier process (QSGW, DMFT, BSE, and BSE-SC) is discussed in Pashov *et al.* [12], and codes are available on the open source electron structure suite Questaal [17]. Expressions we use for the response functions are presented in Ref. [9]. Our all-electronic  $GW$  implementation was adapted from the original ecalj package [18]; the method and basis set are described in detail in

Ref. [12]. For the one-body part a  $k$  mesh of  $12 \times 12 \times 12$  was used; to compute the (much more weakly  $k$  dependent) self-energy, we used a mesh of  $6 \times 6 \times 6$  divisions, employing the tetrahedron method for the susceptibility.

We perform calculations in the tetragonal phases of LFA and CFA; in the CT phase (CT-LFA and CT-CFA) and the corresponding UT phase (UT-LFA and UT-CFA). Structural parameters for each phase are given in the Supplemental Material [19], Table I. The DMFT self-energy, spin and charge susceptibilities, and finally the superconducting instability are computed as a function of temperature. CT-QMC samples more electronic diagrams at reduced temperature and provides insights into the emerging coherence or incoherence in single- and two-particle instabilities; however, it cannot provide knowledge about entrant structural (or structural + magnetic) transitions. On the other hand, it can tell us what would happen if the structural + magnetic transition could be suppressed ( $T_N = 170$  K in CFA), and we can estimate  $T_c$  in the hypothetical UT phase of undoped CFA below  $T_N$ .

In brief, we find that the CT-LFA has no superconducting instability, while UT, CT-CFA, and UT-LFA are all predicted to be superconducting. All of these findings are consistent with experiment. In the experimentally known cases where the systems do superconduct (UT-LFA and CT-CFA), it appears our estimated  $T_c$ 's are a factor of 2 to 3 times larger than the experimental  $T_c$ . A similar discrepancy is observed in estimation of  $T_c$  in doped single-band Hubbard model [14], where it sources from the local approximations of DMFT and needs a better momentum dependent vertex to circumvent this [20]. Apart from a constant scaling, all of these findings are consistent with experiment. Moreover, we find that the hypothetical UT-CFA phase can have the highest  $T_c$  of all. We conclude that UT-CFA would be superconducting if it did not make a transition to an antiferromagnetically ordered state. The superior quality of the QSGW bath combined with nonperturbative DMFT has been shown to possess a high degree of predictive power in one- and two-particle spectral functions [7–9,12] and as in other cases we are able to replicate the experimental observations of spectral functions, including a reasonable estimate for  $T_c$ . The remainder of the Letter uses this machinery to explain what the origins of superconductivity are.

The three systems predicted to have non-negligible  $T_c$  (CT-CFA, UT-LFA, UT-CFA) have two things in common. First, the Fe- $d_{xy}$  state contributes to the hole pocket around the  $\Gamma$  point (Fermi surface is shown in Fig. 1; see also the blue band in Fig. 2). Second, the imaginary part of the spin susceptibility  $\text{Im}\chi(q, \omega)$  has intense peaks centered at  $\mathbf{q} = (\frac{1}{2}, \frac{1}{2}, 0)2\pi/a$ , in the energy window (2,25) meV. The latter is a consequence of the former: low-energy spin-flip transitions involving  $d_{xy}$  are accessible, which give rise to strong peaks in  $\text{Im}\chi(q, \omega)$  around the antiferromagnetic nesting vector  $\mathbf{q}^{\text{AFM}} = (\pi/a, \pi/a, 0)$ .  $\text{Im}\chi(q, \omega)$  is diffused in  $\mathbf{q}$  around  $\mathbf{q}^{\text{AFM}}$ . This broadening

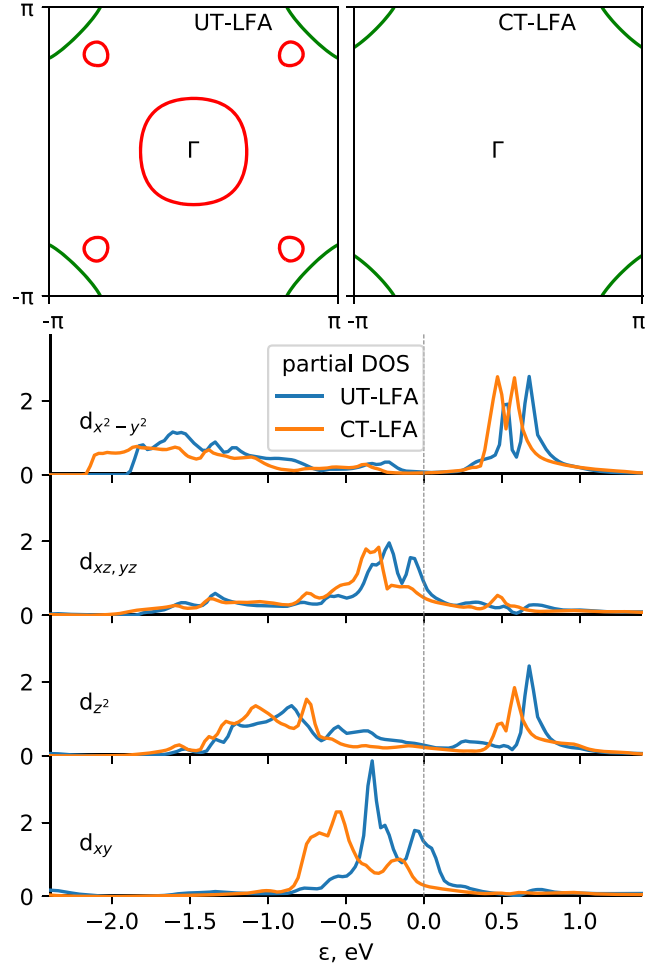


FIG. 1. Fermi surface in the  $k_z = 0$  plane for UT and CT-LFA phases. In the UT phase, the circular pocket around  $\Gamma$  has Fe- $d_{xy}$  character, while chickpea shaped pockets are of Fe- $d_{xz,yz}$  character. These pockets disappear in the CT phase, where superconductivity is absent. Simultaneously, the effective band width  $W$  of the Fe-3d manifold significantly increases in the CT phase ( $\sim 4$  eV, in the UT phase  $W \sim 2.4$  eV, leading to larger electronic itineracy. Also shown is the partial local density of states projected onto the Fe-3d orbitals. The bandwidth  $W$  of narrow  $d_{xy}$  states gets further narrowed in the UT-LFA phase to mark enhancement in effective correlation ( $U/W$ ), where  $U$  is the Hubbard parameter.

in momentum space suppresses antiferromagnetism to allow superconductivity to form. CT-LFA is the only one of the four systems that has negligible instability to superconductivity. In CT-LFA the Fe- $d_{xy}$  state is pushed down (Fig. 2). As a consequence the peak in  $\text{Im}\chi(\mathbf{q}^{\text{AFM}}, \omega)$  occurs at a much higher energy—too high to provide the low-energy glue for Cooper pairs. Also appearing is a pronounced dispersive paramagnon branch around  $q = 0$ . This branch is present in all four systems, but it is strongest in CT-LFA. Nevertheless the *ab initio* calculations predict no superconductivity. This establishes that the paramagnon branch contributes little to the glue for superconductivity in these 122-As based compounds.

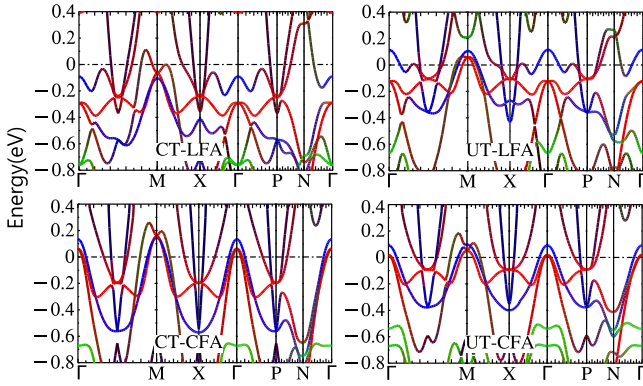


FIG. 2. Color-weighted electronic QSGW band structures in LFA (top) and CFA (bottom). CT (UT) phases are displayed on the left (right). All  $t_{2g}$  Fe states ( $d_{xy}$  in blue,  $d_{xz,yz}$  in red) are in close proximity to the Fermi energy, while the Fe- $d_{eg}$  states (depicted in green) are somewhat below. In the CT phase of LFA, the  $d_{xy}$  state is pushed below  $E_F$ , eliminating the hole pocket at  $\Gamma$  and suppressing  $T_c$ .

Reducing the  $c$  axis in the LFA phase pushes  $d_{xy}$  below the Fermi energy  $E_F$  (top left panel, Fig 2); the remaining hole pocket at  $\Gamma$  is without  $d_{xy}$  character (see Fig 1) [21,22]. Quasiparticles in CT-LFA are much more coherent (see Fig. 3) with small scattering rate  $\Gamma$  (extracted from the imaginary part of the self-energy at  $\omega \rightarrow 0$ ) and large quasiparticle weights  $Z$  relative to the other cases (see Supplemental Material [19], Table II for the orbitally resolved numbers). This further confirms that the CT-LFA

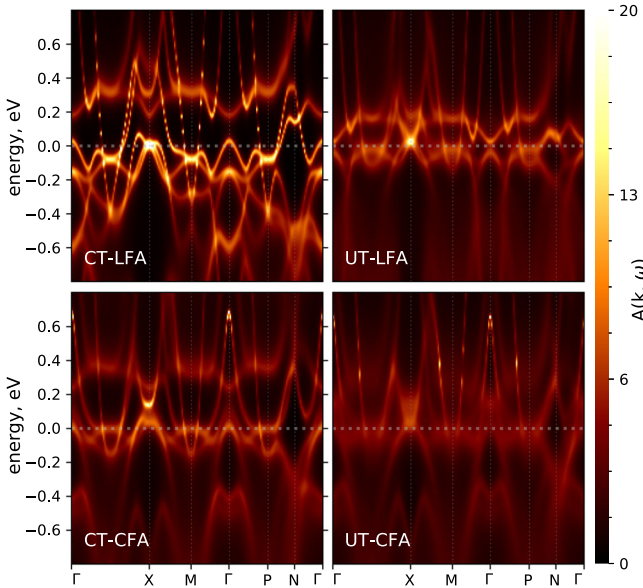


FIG. 3. Single-particle correlated QSGW + DMFT electronic spectral functions  $A(q, \omega)$  for CT and UT phases of LF and CFA along high-symmetry lines. The UT-CFA phase is most incoherent, while the CT-LFA phase is most coherent. The presence (absence) of the Fe- $d_{xy}$  state at Fermi energy appears to be the primary criterion for incoherent (coherent) spectral features.

phase is itinerant with small correlation, using  $U/W$  as a measure. When the  $d_{xy}$  state crosses  $E_F$ , single-particle spectral functions  $A(q, \omega)$  become markedly incoherent. This originates from enhanced single-particle scattering induced by local moment fluctuations within DMFT and suppressed orbitally resolved  $Z$  (Supplemental Material [19], Table II). In the superconducting cases the  $d_{xy}$  orbital character is the primary source of incoherence with high scattering rate ( $\Gamma > 60$  meV) and quasiparticle weight as low as  $\sim 0.4$ .

The peak in  $\text{Im}\chi(\mathbf{q}^{\text{AFM}}, \omega)$  can be observed in almost all iron based superconductors [15,23]. However, what varies significantly over various systems is the dispersion of the branches. The less itinerant the system is, the smaller dispersion in  $\text{Im}\chi(q, \omega)$  (and typical spin exchange scale  $J \sim t^2/U$ ), and it is more strongly correlated.

In the UT-LFA phase,  $\text{Im}\chi(q, \omega)$  has a dispersive magnon branch extending to  $\sim 70$  meV. As can be observed in Fig. 4, both the branch and the low-energy peak at  $(\frac{1}{2}, \frac{1}{2}, 0)$  are significantly broad. The dispersion is significantly smaller than in undoped  $\text{BaFe}_2\text{As}_2$  (BFA) [24], dispersion survives up to 200 meV at  $(\frac{1}{2}, 0, 0)$ . This suppression of branches and concomitant broadening suggests that UT-LFA is more correlated than BFA. In contrast with UT-LFA, CT-LFA has a Stoner-like continuum of spin excitations (in the figure the intensity is scaled by a factor of 5 to make it similar to the UT phase) without any well-defined low energy peak. Similar spin excitations can be observed in the phosphorus compounds ( $\text{BaFe}_2\text{P}_2$ ,  $\text{LiFeP}$ ) where the system either does not superconduct or  $T_c$  is fairly low (when it does) [15]. These are

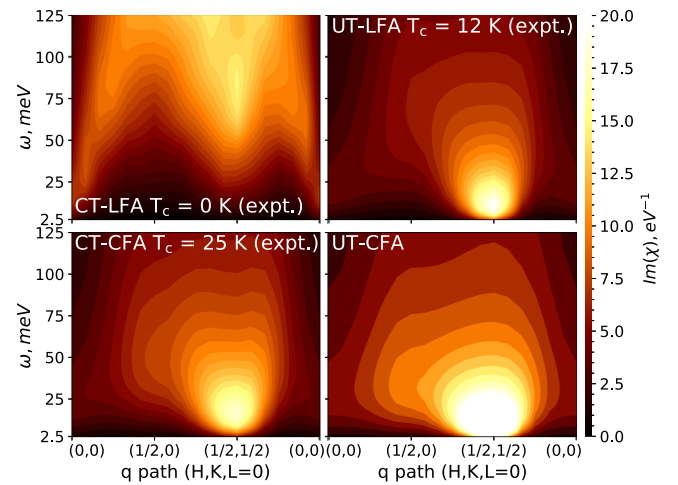


FIG. 4. The energy and momentum resolved spin susceptibility  $\text{Im}\chi(q, \omega)$  (in the top panel from left to right) shown for the CT and UT phases, respectively. The  $q$  path ( $H, K, L = 0$ ) is chosen along  $(0, 0) - (\frac{1}{2}, 0) - (\frac{1}{2}, \frac{1}{2}) - (0, 0)$  in the Brillouin zone corresponding to the two-Fe atom unit cell. The intensity in the CT phase is artificially multiplied by 5 to bring excitations for CT and UT phases to the same scale.

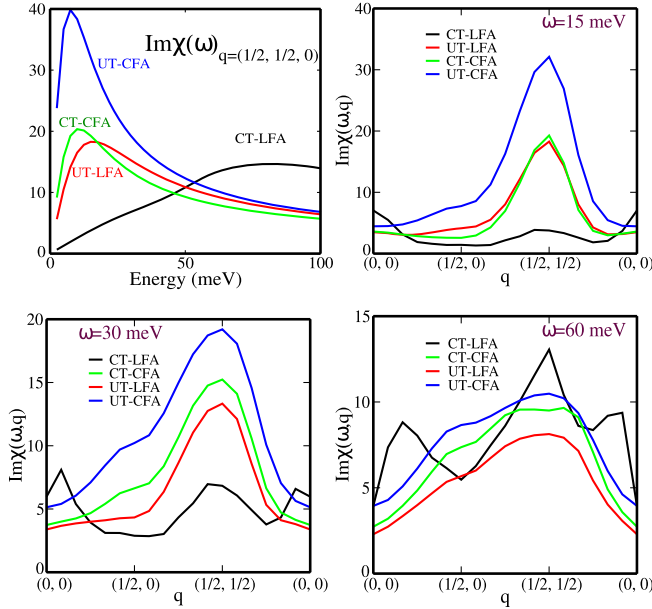


FIG. 5. The low energy behavior of  $\text{Im}\chi(q, \omega)$  is shown for four candidates at  $q = (\frac{1}{2}, \frac{1}{2}, 0)$ . The more intense the peak is, higher is the  $T_c$ . Three different energy cuts at 15, 30, and 60 meV for  $\text{Im}\chi(q, \omega)$  are resolved along the  $q$  path  $(H, K, L = 0) = (0, 0) - (\frac{1}{2}, 0) - (\frac{1}{2}, \frac{1}{2}) - (0, 0)$  to stress the low-energy concentration of glue in the superconducting phases. (The intensity of CT-LFA peak is artificially multiplied by five to bring excitations for CT and UT phases to the same scale).

among the most itinerant systems of all iron based superconductors and both the quasiparticle and spin excitations are bandlike. In both the phases we find weak to no  $q_z$  dispersion of the susceptibilities, making the spin fluctuations effectively two dimensional.

In Fig. 5 we compare  $\text{Im}\chi(q, \omega)$  at  $(\frac{1}{2}, \frac{1}{2}, 0)$  for four candidates. The UT-CFA has most intense low energy peak followed by CT-CFA and UT-LFA. Low energy spin excitations for CT-LFA is gapped at  $(\frac{1}{2}, \frac{1}{2}, 0)$ . Further, we take three energy cuts of  $\text{Im}\chi(q, \omega)$  at  $\omega = 15, 30, 60$  meV along the path  $(H, K, L = 0) = (0, 0) - (\frac{1}{2}, 0) - (\frac{1}{2}, \frac{1}{2}) - (0, 0)$ . At 15 meV, the UT-CFA peak is significantly stronger than the rest; CT-LFA has weak uniform spin excitation at  $q = 0$ , and is almost entirely suppressed at  $(\frac{1}{2}, \frac{1}{2}, 0)$ . It appears that an intense low energy peak which is simultaneously broadened in momentum space provides maximum favorable glue for superconducting ordering. For higher energy  $\omega = 30$  and 60 meV, cuts the sharp difference between UT-CFA and others start to diminish and the spin excitations for all systems become broad and incoherent and nearly comparable. CT-LFA shows a clear two-peak structure associated with the high energy paramagnon branch and it disperses to  $\sim 500$  meV (see Supplemental Material [19]). The eigenvalues and eigenfunctions of superconducting susceptibilities, superconducting pairing symmetries cannot be extracted from

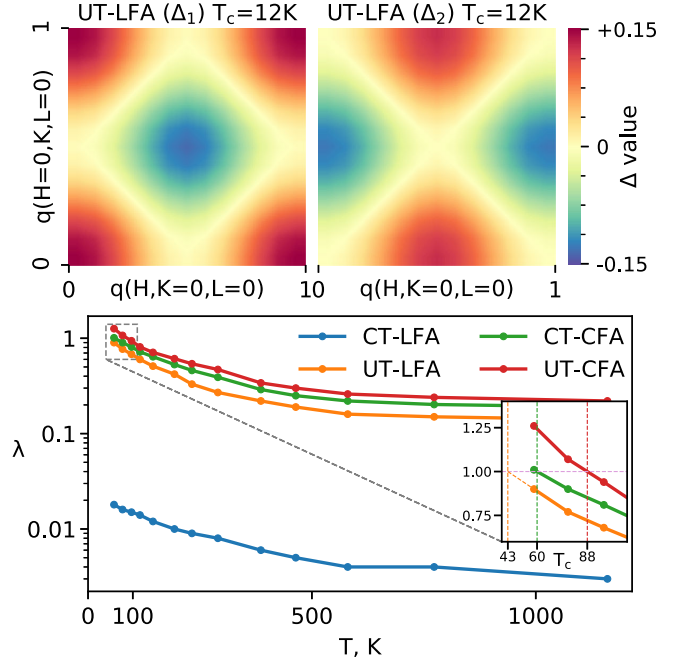


FIG. 6. The superconducting instability is absent in the CT-LFA phase. The superconducting instability corresponding to the leading ( $\lambda_1$ ) and lagging ( $\lambda_2$ ) eigenvalues of the solutions to the linearized Eliashberg equations,  $\Delta(q, \omega = 0)$  are shown for the UT-LFA phase. The evolution of the leading eigenvalue as a function of temperature is shown for CT-CFA, UT-CFA, and UT-LFA in the bottom panel. In the inset we enlarge the low temperature part of the curves to show the estimated  $T_c$ 's.

the spin dynamics alone. We compute the full two particle scattering amplitude in the particle-particle channel within our DMFT framework, and we solve Eliashberg equations in the BCS low energy approximation [9,14,15]. We resolve our eigenfunctions of the gap equation into different inter- and intra-orbital channels, and observe the trend in the leading eigenvalues with temperature in both CT and UT phases. We observe that there are two dominant eigenvalues of the gap equation. The eigenvalues increase with decreasing T in the UT-LFA, UT-CFA, and CT-CFA, while they are vanishingly small (at least 1 order of magnitude smaller than the UT phase) and (in the CT-LFA phase) insensitive to T. The corresponding eigenfunctions in the UT-LFA phase have extended  $s$ -wave (leading eigenfunction  $\Delta_1$  for eigenvalue  $\lambda_1$ ) and  $d_{x^2-y^2}$  (lagging eigenfunction  $\Delta_2$  for eigenvalue  $\lambda_2$ ) characters (see Fig. 6). We also find that these instabilities are primarily in the intra-orbital  $d_{xy} - d_{xy}$  channel and the interorbital components are negligible. In both the UT and CT-CFA phases the only instability appears to be of extended  $s$ -wave nature. We track the temperature at which the superconducting susceptibility diverges (the leading eigenvalue approaches one) to estimate  $T_c$  (see Fig. 6). We find that the pairing vertex  $\Gamma$  rises steeply with lowering temperatures and the leading eigenvalue  $\lambda$  follows the temperature dependence of

$\Gamma$  (see Supplemental Material [19]). Suppression of the charge component of  $\Gamma$  leads to no qualitative change to the temperature dependence of  $\lambda$  and only weakly changes its magnitude (see Supplemental Material [19]). Our results suggest that  $T_c$  is directly proportional to the strength of the low energy peak at  $(\frac{1}{2}, \frac{1}{2})$ , which is further controlled by the correlations and scattering in the Fe- $3d_{xy}$  state. The importance of  $d_{xy}$  state was identified in a recent experimental study of Fano-effects in  $\text{Ba}_{1-x}\text{K}_x\text{Fe}_2\text{As}_2$  [25].

To conclude, we establish the interplay between the band structure and correlations that lead to emergence (suppression) of superconductivity in the UT-LFA (CT-LFA) phase. We establish a direct correspondence between the proximity of the  $d_{xy}$  state to the Fermi energy, and show that it contributes to enhanced low energy scattering and significantly incoherent quasiparticles. Incoherence affects two-particle features: the spin susceptibilities also show broad and intense low energy spin fluctuations centered at  $(\frac{1}{2}, \frac{1}{2})$ . As the phase is quenched, in CT-LFA,  $d_{xy}$  is pushed below  $E_F$ , which causes coherent spectral features to emerge with a broad continuum of spin excitations. These do not provide glue conducive for Cooper pair formation. Our conclusions find further validation in our calculations in UT and CT phases in CFA. UT-CFA was found to have the most intense low energy susceptibility peak among the four candidates and is predicted to have the highest, were the superconducting instability not suppressed by entrant first order structural transition.

This work was supported by the Simons Many-Electron Collaboration. We acknowledge PRACE for awarding us access to SuperMUC at GCS@LRZ, Germany, STFC Scientific Computing Department's SCARF cluster, Cambridge Tier-2 system operated by the University of Cambridge Research Computing Service ([www.hpc.cam.ac.uk](http://www.hpc.cam.ac.uk)) funded by EPSRC Tier-2 capital Grant No. EP/P020259/1.

\*swagata.acharya@kcl.ac.uk

- [1] A. Iyo, S. Ishida, H. Fujihisa, Y. Gotoh, I. Hase, Y. Yoshida, H. Eisaki, and K. Kawashima, *J. Phys. Chem. Lett.* **10**, 1018 (2019).
- [2] D.-Y. Chen, J. Yu, B.-B. Ruan, Q. Guo, L. Zhang, Q.-G. Mu, X.-C. Wang, B.-J. Pan, G.-F. Chen, and Z.-A. Ren, *Chin. Phys. Lett.* **33**, 067402 (2016).
- [3] Q. Huang, Y. Qiu, W. Bao, M. A. Green, J. W. Lynn, Y. C. Gasparovic, T. Wu, G. Wu, and X. H. Chen, *Phys. Rev. Lett.* **101**, 257003 (2008).
- [4] N. Ni, S. Nandi, A. Kreyssig, A. I. Goldman, E. D. Mun, S. L. Bud'ko, and P. C. Canfield, *Phys. Rev. B* **78**, 014523 (2008).
- [5] M. S. Torikachvili, S. L. Bud'ko, N. Ni, and P. C. Canfield, *Phys. Rev. Lett.* **101**, 057006 (2008).
- [6] A. Kreyssig, M. A. Green, Y. Lee, G. D. Samolyuk, P. Zajdel, J. W. Lynn, S. L. Bud'ko, M. S. Torikachvili, N. Ni, S. Nandi, J. B. Leão, S. J. Poulton, D. N. Argyriou, B. N. Harmon, R. J. McQueeney, P. C. Canfield, and A. I. Goldman, *Phys. Rev. B* **78**, 184517 (2008).
- [7] L. Sponza, P. Pisanti, A. Vishina, D. Pashov, C. Weber, M. van Schilfhaarde, S. Acharya, J. Vidal, and G. Kotliar, *Phys. Rev. B* **95**, 041112(R) (2017).
- [8] S. Acharya, C. Weber, E. Plekhanov, D. Pashov, A. Taraphder, and M. Van Schilfhaarde, *Phys. Rev. X* **8**, 021038 (2018).
- [9] S. Acharya, D. Pashov, C. Weber, H. Park, L. Sponza, and M. Van Schilfhaarde, *Commun. Phys.* **2**, 1 (2019).
- [10] E. Baldini, M. A. Sentef, S. Acharya, T. Brumme, E. Sheveleva, F. Lyzwa, E. Pomjakushina, C. Bernhard, M. van Schilfhaarde, F. Carbone, A. Rubio, and C. Weber, *Proc. Natl. Acad. Sci. U.S.A.* **117**, 6409 (2020).
- [11] J. Tomczak, P. Liu, A. Toschi, G. Kresse, and K. Held, *Eur. Phys. J. Special Topics* **226**, 2565 (2017).
- [12] D. Pashov, S. Acharya, W. R. Lambrecht, J. Jackson, K. D. Belashchenko, A. Chantis, F. Jamet, and M. van Schilfhaarde, *Comput. Phys. Commun.* **249**, 107065 (2020).
- [13] T. Kotani, M. van Schilfhaarde, and S. V. Faleev, *Phys. Rev. B* **76**, 165106 (2007).
- [14] H. Park, Ph.D. thesis, Rutgers University-Graduate School-New Brunswick, 2011.
- [15] Z. Yin, K. Haule, and G. Kotliar, *Nat. Phys.* **10**, 845 (2014).
- [16] E. Şaşıoğlu, C. Friedrich, and S. Blügel, *Phys. Rev. B* **83**, 121101 (2011).
- [17] Questaal website, <https://www.questaal.org>.
- [18] ecalj package, <https://github.com/tkotani/ecalj/>.
- [19] See Supplemental Material at <http://link.aps.org/supplemental/10.1103/PhysRevLett.124.237001> includes input structural parameters for our calculations,  $U$  and  $J$  computed from C-RPA, orbitally resolved quasi-particle weight and scattering rates in different compounds, magnetic susceptibilities resolved over larger energy window and a detailed description of the methods implemented for computing  $T_c$ .
- [20] M. Kitatani, T. Schäfer, H. Aoki, and K. Held, *Phys. Rev. B* **99**, 041115(R) (2019).
- [21] I. I. Mazin, M. Shimizu, N. Takemori, and H. O. Jeschke, *Phys. Rev. Lett.* **123**, 267001 (2019).
- [22] H. Usui and K. Kuroki, *Phys. Rev. Research* **1**, 033025 (2019).
- [23] Z. Yin, K. Haule, and G. Kotliar, *Nat. Mater.* **10**, 932 (2011).
- [24] L. W. Harriger, H. Q. Luo, M. S. Liu, C. Frost, J. P. Hu, M. R. Norman, and P. Dai, *Phys. Rev. B* **84**, 054544 (2011).
- [25] B. Xu, *et al.*, *Phys. Rev. Lett.* **122**, 217002 (2019).